








Variation of Magnetic Flux Ropes through Major Solar Flares

Aiying Duan^{1,2} , Chaowei Jiang³ , Zhenjun Zhou^{1,4} , Xueshang Feng³ , and Jun Cui^{1,4} 

¹ School of Atmospheric Sciences, Sun Yat-sen University, Zhuhai 519000, People's Republic of China; duanaiy@mail.sysu.edu.cn

² School of Space and Environment, Beihang University, Beijing, 100191, People's Republic of China

³ Institute of Space Science and Applied Technology, Harbin Institute of Technology, Shenzhen 518055, People's Republic of China

⁴ CAS Center for Excellence in Comparative Planetology, People's Republic of China

Received 2020 December 7; revised 2020 December 20; accepted 2020 December 22; published 2021 January 25

Abstract

It remains unclear how solar flares are triggered and in what conditions they can be eruptive with coronal mass ejections. Magnetic flux ropes (MFRs) has been suggested as the central magnetic structure of solar eruptions, and their ideal instabilities, including the kink instability (KI) and torus instability (TI), are important candidates for triggering mechanisms. Here, using magnetic field extrapolations from observed photospheric magnetograms, we systematically studied the variation of coronal magnetic fields, focusing on MFRs, through major flares including 29 eruptive and 16 confined events. We found that nearly 90% of events possess MFRs before flares, and 70% have MFRs even after flares. We calculated the controlling parameters of KI and TI, including the MFR's maximum twist number and the decay index of its strapping field. Using the KI and TI thresholds empirically derived solely from the pre-flare MFRs, two distinctly different regimes are shown in the variation of the MFR controlling parameters through flares. For the events with both parameters below their thresholds before flares, we found no systematic change of the parameters after the flares, in either the eruptive or confined events. In contrast, for the events with any of the two parameters exceeding their threshold before flares (most of them are eruptive), there is systematic decrease in the parameters to below their thresholds after flares. These results provide a strong constraint for the values of the instability thresholds and also stress the necessity of exploring other eruption mechanisms in addition to the ideal instabilities.

Unified Astronomy Thesaurus concepts: [Solar coronal mass ejections \(310\)](#); [Solar flares \(1496\)](#); [Solar active regions \(1974\)](#)

1. Introduction

Solar eruptions, often referred to as explosive phenomena in the solar atmosphere, are the leading driver of disastrous space weather. The two most common forms of solar eruptions are solar flares and coronal mass ejections (CMEs), which are often (but not always) closely related with each other. Both of them are believed to be caused by a drastic release of free energy stored in the complex, unstable magnetic field in the solar corona. Prediction of such eruptions is difficult because there are many important issues of the underlying physics that remain unresolved. For instance, both the structure of the coronal magnetic field prior to eruption and the triggering mechanism of the eruption are still undetermined; the key factor that causes the difference between eruptive flares (flares accompanied by CMEs) and confined flares (flares without CMEs) is still unclear.

Competing models of solar eruptions have been proposed based on either resistive magnetohydrodynamics (MHD), i.e., magnetic reconnection, or ideal MHD instabilities (e.g., see reviews of Forbes et al. 2006; Shibata & Magara 2011; Schmieder & Aulanier 2012; Schmieder et al. 2013; Aulanier 2014; Janvier et al. 2015). For example, in the reconnection-based models, such as the runaway tether-cutting reconnection (Moore et al. 2001) and the breakout reconnection (Antiochos et al. 1999), it is assumed that before the flare the magnetic field has a strongly sheared configuration, and eruption is triggered by magnetic reconnection that is followed by a positive feedback between reconnection and outward expansion of the sheared magnetic flux. However, it is difficult to determine in what conditions the feedback can be

established, and therefore developing prediction methods based on these models is not easy.

On the other hand, the ideal MHD instabilities, mainly the helical kink instability (KI; Hood & Priest 1981; Török et al. 2004, 2010; Török & Kliem 2005) and the torus instability (TI; Bateman 1978; Kliem & Török 2006) are developed based on magnetic flux rope (MFR; Kuperus & Raadu 1974; Chen 1989; Titov & Démoulin 1999; Liu 2020), which is a coherent group of twisted magnetic flux winding around a common axis. In the MFR-based models, it is assumed that MFR exists in the corona prior to eruption. Then the pre-existing MFR is slowly driven to an unstable regime by motions in the lower atmosphere (the photosphere) and is triggered to erupt through either KI or TI. The twist degree of the MFR itself and the decay index of the MFR's strapping field (Török & Kliem 2005, 2007; Kliem & Török 2006) are two critical parameters that control the KI and TI, respectively, and instabilities occur when they exceed some values, i.e., the instability thresholds. Thus, the controlling parameters of the instabilities could potentially be used in forecasting solar eruptions, which is a unique advantage of the ideal MHD models. To this end, it is crucial to identify the MFRs in the coronal magnetic field and to precisely determine the thresholds of the instabilities.

However, there appears to be no single value for the thresholds, and different studies, from either analytic, numerical, or even laboratory investigations, often produce discrepant results. For instance, the KI threshold T_w , which measures the winding number of magnetic field lines around the MFR's axis, is found to range from ~ 1.25 turns to ~ 2.5 turns in previous analytic and numerical investigations (Hood & Priest 1981;

Baty 2001; Fan & Gibson 2003; Török & Kliem 2003, 2005). This is because it depends on the details of the MFR, such as the line-tying effects by the photosphere, the aspect ratio of the MFR (i.e., ratio of the rope’s length to its cross-section size), and the geometry of the axis. The TI controlling parameter, i.e., the decay index n , refers to the spatial decreasing speed of the MFR’s overlying magnetic field that straps the MFR. A series of theoretical and numerical studies (Kliem & Török 2006; Fan & Gibson 2007; Török & Kliem 2007; Aulanier et al. 2010; Démoulin & Aulanier 2010; Fan 2010; Zuccarello et al. 2015) show that the TI threshold of decay index has typical values in the domain of $1.1 \sim 2$, while some laboratory experiments suggest that it might be as low as $0.65 \sim 1.1$ (Myers et al. 2015; Alt et al. 2020), depending mainly on the ratio of the apex height and footpoint half-separation.

Furthermore, due to the intrinsic complexity of the magnetic field in the solar corona, the configuration of MFRs can be very different from case to case, which may not be fully characterized by the KI and TI theories that are derived based on a relatively simplified or idealized configuration in previous analytic, numerical, and laboratory investigations. In some cases, if the filaments have significant rotational motions; they tend to be associated with failed eruptions despite the decay index satisfying the threshold for TI (Zhou et al. 2019). Recently, statistical studies based on magnetic field extrapolation have been employed to study configurations of coronal MFRs, focusing on the two controlling parameters in the hope of finding more realistic thresholds that can be used for prediction and to differentiate the types of eruptive and confined flares. Using a nonlinear-force-free field (NLFFF) extrapolation code developed by Wiegmann (2004) based on the optimization method, Jing et al. (2018) surveyed the pre-flare coronal magnetic field for 38 major flares, and they found that only the TI plays an important role in distinguishing the different types of flares, with the threshold of decay index found to be ~ 0.75 , which is much lower than the canonical value of 1.5 (Kliem & Török 2006). The twist numbers show no systematic difference between the confined and eruptive events. Then, Duan et al. (2019) performed a similar survey of 45 major flares with the pre-flare force-free magnetic field reconstructed by another NLFFF extrapolation method, the CESE–MHD–NLFFF code, which is based on the MHD-relaxation method (Jiang & Feng 2013). They used a more strict definition of MFR that refers to field lines with winding number of at least one full turn, and found that $\sim 90\%$ of the events possess pre-flare MFRs but with very different 3D structures. Quite different from the results in Jing et al. (2018), the newer study found the KI and TI thresholds to be $|T_w|_{\text{crit}} \sim 2$ and $n_{\text{crit}} \sim 1.3$, respectively, which are close to values derived in theoretical studies, and KI and TI play a nearly equally important role in discriminating the eruptive and confined flares.

The two previous studies have only analyzed the pre-flare magnetic fields. In this Letter, we investigate for the first time the variations of MFRs, focusing on changes of the two controlling parameters of KI and TI, from immediately pre-flare to post-flare states. For comparison, we use the same events studied in Duan et al. (2019) and thus the CESE–MHD–NLFFF code is employed to reconstruct both the pre-flare and post-flare coronal magnetic fields. It is found that the existences of post-flare MFRs is also very common, even for the eruptive flares, suggesting that the pre-flare MFR often does not expel

out entirely. Furthermore, a key difference of the variation of the controlling parameters from before to after flare is shown in two different regimes of events defined by the KI and TI thresholds derived in our previous study. These results provide a strong constraint for the values of the instability thresholds, and confirm that the events with pre-flare parameters exceeding the thresholds are very likely triggered by the ideal instabilities. For those with the two parameters below the thresholds, which account for more than half of all the events, other mechanisms such as the reconnection-based ones should be considered.

2. Data and Method

We have investigated 29 eruptive flares (above GOES-class M5) and 16 confined ones (above M3.9) observed by the Solar Dynamic Observatory (SDO; Pesnell et al. 2012) from 2011 January to 2017 December, which are listed in Table 1. All the 45 events occurred within 45° in longitude of the disk center, and most of them are active region (AR) flares (see more details of the criterion for selecting events in Duan et al. 2019). Based on the vector magnetograms from the Helioseismic and Magnetic Imager (HMI; Hoeksema et al. 2014) on board SDO, the CESE–MHD–NLFFF code (Jiang & Feng 2013) was used to reconstruct a pre-flare 3D coronal magnetic field and a post-flare one for each event. For the pre-flare reconstruction, we used the last available data for at least 10 minutes before the flare start time to avoid the possible artifacts introduced by the strong flare emission, while for the post-flare field, we used the first available magnetogram at least 1 hr after the flare peak, a time when the post-flare field relaxed to nearly MHD equilibrium but without significant further stressing by the photospheric motions. The vector magnetograms are obtained from the Space-weather HMI Active Region Patch (Bobra et al. 2014) data product.

Following the same procedure introduced in Duan et al. (2019), we first search for MFRs in the full reconstruction volume based on the volumetric distribution of the magnetic twist number T_w (Berger & Prior 2006), which can provide a good approximation of the winding turns of two infinitesimally close field lines about each other. T_w is defined for closed field lines (whose two footpoints are anchored in the photosphere) as

$$T_w = \int_L \frac{(\nabla \times \mathbf{B}) \cdot \mathbf{B}}{4\pi B^2} dl \quad (1)$$

where the integral is taken along the field lines. We calculate T_w on grid points with a resolution of 4 times of the original data, and define the MFR as a coherent group of magnetic field lines with T_w of the same sign and $|T_w| \geq 1$. Thus an MFR approximately has all field lines with winding around the axis at least one full turn, which is a strict definition. Moreover, the MFRs as found with the T_w distribution are further selected by restricting them within the flare sites, e.g., through comparing with SDO/Atmospheric Imaging Assembly (AIA) observable filaments and flare ribbons in the flare site. One may refer to Duan et al. (2019) for more information about the definition and selection of MFRs. Both Liu et al. (2016) and Duan et al. (2019) suggested that the maximum value of $|T_w|$ can be regarded as a reliable proxy of the MFR axis, and they also pointed out that the $|T_w|_{\text{max}}$ has a very sensitive association with KI occurring in flares. Thus we employ the $|T_w|_{\text{max}}$ as the KI controlling parameter.

Table 1
List of Events and Parameters of Their Pre- and Post-flare MFRs

No.	Flare Peak Time	Flare Class	NOAA AR	Position	E/C ^a	T_w Before ^b	n Before	T_w After ^c	n After
1	SOL2011-02-13T17:38	M6.6	11158	S20E04	E	0.76	0.99	0.55	1.25
2	SOL2011-02-15T01:56	X2.2	11158	S20W10	E	1.52	0.98	0.86	0.69
3	SOL2011-03-09T23:23	X1.5	11166	N08W09	C	-1.75	0.50	-1.45	0.30
4	SOL2011-07-30T02:09	M9.3	11261	S20W10	C	-0.88	0.51	-0.80	1.48
5	SOL2011-08-03T13:48	M6.0	11261	N16W30	E	2.45	1.40	1.68	1.14
6	SOL2011-09-06T01:50	M5.3	11283	N14W07	E	0.92	0.52	1.30	0.40
7	SOL2011-09-06T22:20	X2.1	11283	N14W18	E	1.02	1.65	0.89	0.17
8	SOL2011-10-02T00:50	M3.9	11305	N12W26	C	-0.92	0.42	-0.92	0.20
9	SOL2012-01-23T03:59	M8.7	11402	N28W21	E	-1.63	0.73	-1.40	1.17
10	SOL2012-03-07T00:24	X5.4	11429	N17E31	E	-2.11	0.71	-1.96	0.98
11	SOL2012-03-09T03:53	M6.3	11429	N15W03	E	-1.17	0.73	-1.38	0.61
12	SOL2012-05-10T04:18	M5.7	11476	N12E22	C	-1.11	1.21	-0.77	1.11
13	SOL2012-07-02T10:52	M5.6	11515	S17E08	E	-1.56	0.35	-1.25	0.15
14	SOL2012-07-05T11:44	M6.1	11515	S18W32	C	1.14	-0.41	1.14	-0.03
15	SOL2012-07-12T16:49	X1.4	11520	S15W01	E	2.20	0.42	1.83	0.28
16	SOL2013-04-11T07:16	M6.5	11719	N09E12	E	-1.10	0.26	-2.00	0.09
17	SOL2013-10-24T00:30	M9.3	11877	S09E10	E	2.00	0.56	1.50	0.42
18	SOL2013-11-01T19:53	M6.3	11884	S12E01	C	1.50	0.42	1.60	1.40
19	SOL2013-11-03T05:22	M4.9	11884	S12W17	C	3.00	0.07	2.10	0.27
20	SOL2013-11-05T22:12	X3.3	11890	S12E44	E	1.35	2.72	1.10	1.57
21	SOL2013-11-08T04:26	X1.1	11890	S12E13	E	1.26	1.87	0.80	0.49
22	SOL2013-12-31T21:58	M6.4	11936	S15W36	E	-2.20	1.11	-1.65	0.67
23	SOL2014-01-07T10:13	M7.2	11944	S13E13	C	1.65	0.21	0.88	0.39
24 ^d	SOL2014-01-07T18:32	X1.2	11944	S15W11	E	6.50	0.20	3.86	0.31
25	SOL2014-02-02T09:31	M4.4	11967	S10E13	C	-1.73	-0.12	-1.81	-0.04
26	SOL2014-02-04T04:00	M5.2	11967	S14W06	C	-1.90	1.03	-1.68	0.96
27	SOL2014-03-29T17:48	X1.1	12017	N10W32	E	1.53	1.72	0.60	1.37
28	SOL2014-04-18T13:03	M7.3	12036	S20W34	E	2.30	1.82	1.60	0.49
29	SOL2014-09-10T17:45	X1.6	12158	N11E05	E	-0.85	0.17	-1.31	0.16
30 ^d	SOL2014-09-28T02:58	M5.1	12173	S13W23	E	-2.76	1.96	-2.00	0.57
31	SOL2014-10-22T14:28	X1.6	12192	S14E13	C	-1.10	0.94	-0.99	0.91
32	SOL2014-10-24T21:41	X3.1	12192	S22W21	C	-1.79	0.64	-1.55	0.50
33	SOL2014-11-07T17:26	X1.6	12205	N17E40	E	3.55	1.21	1.60	0.51
34	SOL2014-12-04T18:25	M6.1	12222	S20W31	C	2.60	0.60	1.86	0.65
35	SOL2014-12-17T04:51	M8.7	12242	S18E08	E	0.70	0.66	0.71	0.58
36	SOL2014-12-18T21:58	M6.9	12241	S11E15	E	1.09	1.49	1.00	0.27
37	SOL2014-12-20T00:28	X1.8	12242	S19W29	E	1.32	0.56	1.18	0.53
38	SOL2015-03-11T16:21	X2.1	12297	S17E22	E	2.04	1.80	1.29	0.51
39	SOL2015-03-12T14:08	M4.2	12297	S15E06	C	1.10	0.72	1.30	0.99
40	SOL2015-06-22T18:23	M6.5	12371	N13W06	E	-1.24	1.51	-0.93	1.37
41	SOL2015-06-25T08:16	M7.9	12371	N12W40	E	-2.90	0.49	-2.10	0.56
42	SOL2015-08-24T07:33	M5.6	12403	S14E00	C	1.04	0.33	0.73	0.36
43	SOL2015-09-28T14:58	M7.6	12422	S20W28	C	-1.25	1.20	-1.25	1.06
44	SOL2017-09-04T20:33	M5.5	12673	S10W11	E	-1.43	1.09	-1.45	0.49
45	SOL2017-09-06T12:02	X9.3	12673	S09W34	E	-1.80	1.72	-1.10	0.22

Notes.^a E—eruptive, C—confined.^b Before flare—based on the last available magnetogram for at least 10 minutes before the flare GOES start time.^c After flare—based on the first available magnetogram at least 1 hr after the flare peak time.^d Event 24 occurred between NOAA ARs 11944 and 11943, and event 30 occurred between ARs 12173 and 12172.

As aforementioned, TI is controlled by the decay index of the strapping field of the MFR. In much of the literature, the decay index is simply defined as along the vertical or radial direction. However, nonradial eruptions are frequently observed in filament eruptions (McCauley et al. 2015). Thus, in this Letter, the decay index is calculated along an oblique line matching the direction of the eruption. In a configuration where the MFR significantly deviates from the vertical direction, we use a slice cutting through the middle of the rope axis (often at its apex, marked as P) perpendicularly, and the slice intersects with the bottom polarity inversion line (PIL)

on the point marked as O. OP is the oblique line directing from O to P. The strapping magnetic field is extrapolated from the B_z component of the photospheric magnetogram with the potential field model. Then, it is decomposed into three orthogonal components B_e , B_p , and B_t , where B_e is along OP, B_p is perpendicular to the OP on the slice, and B_t is perpendicular to the slice (one can refer to Figure 2 in Duan et al. 2019). Among them, only the cross product between the current of the rope and the poloidal flux B_p can produce an effective strapping force directing P to O, because B_t is parallel to the current of the rope, and the cross product of the current with B_e produces

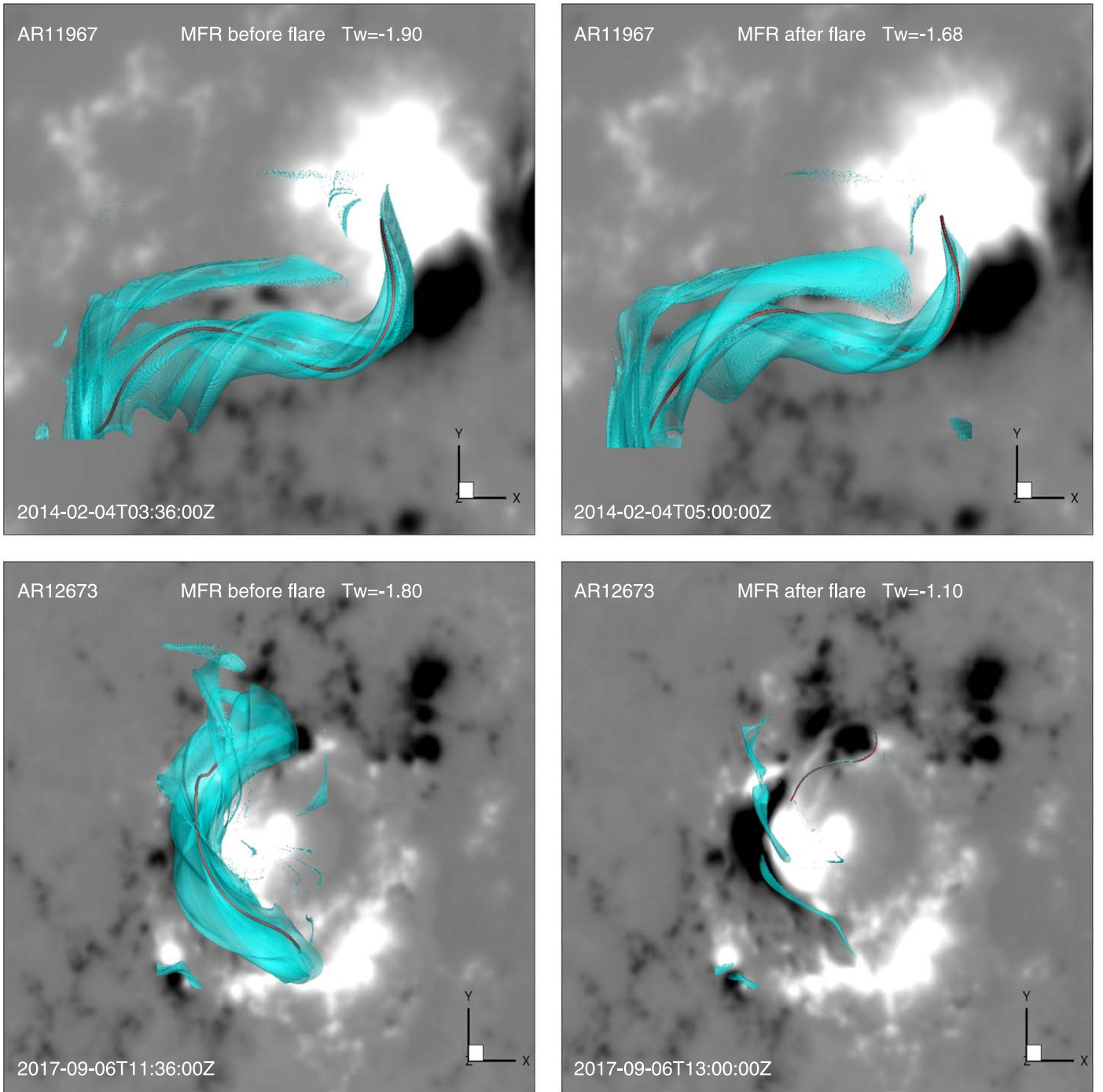


Figure 1. Two examples showing the MFRs before (left panels) and after (right panels) flares. The top panels show the results for an M5.2 confined flare (event 26) on 2014 February 4 in AR 11967. The bottom panels show results for an X9.3 eruptive flare (event 45) on 2017 September 6 in AR 12673. In all the panels, the transparent cyan 3D object is the isosurface of the $|T_w| = 1$, showing the surface of the MFRs. Embedded in the isosurface is the axis of the MFR, which is denoted by the thick red line. The MFR axis possesses the maximum of $|T_w|$, which is denoted on each panel. The background images show the magnetic flux distribution on the photosphere with the positive flux colored in white and negative flux in black.

a force parallel to B_p , which can only control the eruption direction, as B_e often has a small value. Thus, to be more relevant, we define the decay index n as

$$n = \frac{d \log(B_p)}{d \log(r)} \quad (2)$$

where r is the distance pointing from O to P.

3. Results

Our previous survey (Duan et al. 2019), which was based on only the pre-eruption magnetic fields, found that 39 of the 45 events possess pre-flare MFRs, and suggested that the lower limits for TI and KI thresholds are $n_{\text{crit}} = 1.3$ and $|T_w|_{\text{crit}} = 2$, respectively, because 90% of events (11 in 13 events) with $|T_w| \geq 2$ erupted and all events (11 events) with $n \geq 1.3$ erupted. Thus, it seems that KI and TI play a nearly equally important role in discriminating the eruptive and confined

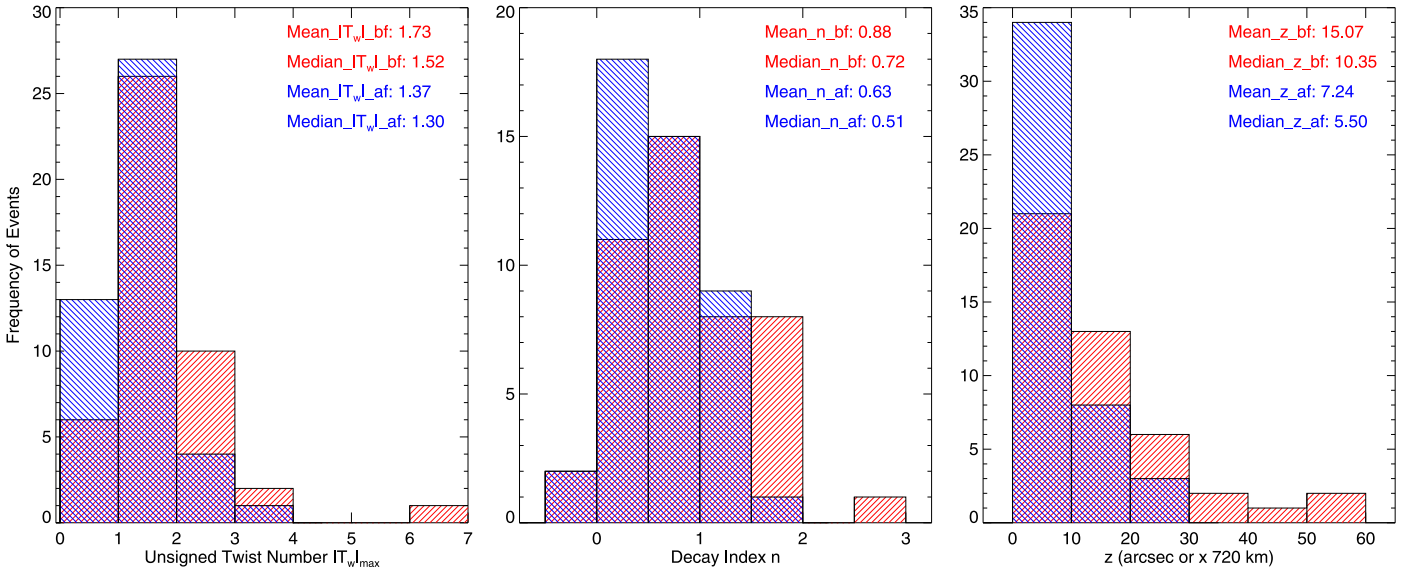


Figure 2. Histogram of the twist number $|T_w|_{\max}$, the decay index n , and the apex height of magnetic field rope axis z_{\max} . The red and blue boxes denote the period before and after the flares, respectively. The average and median values for all the parameters are denoted in each panel.

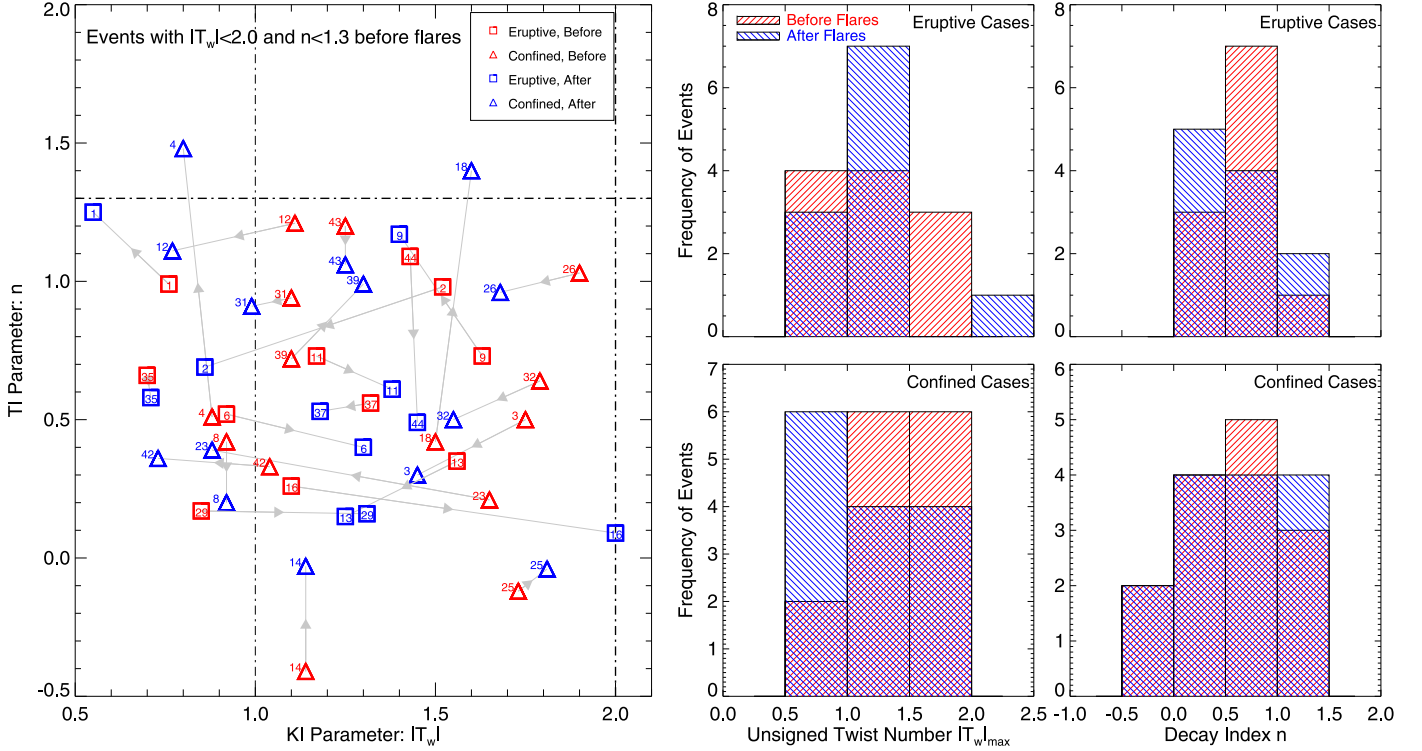


Figure 3. Left panel: scatter diagram of decay index n (TI parameter) vs. $|T_w|_{\max}$ (KI parameter) for events with $|T_w| < 2.0$ and $n < 1.3$ before flares. The boxes (triangles) denote eruptive (confined) flares, the red (blue) color denotes before (after) flares, and the number of the events is marked within or neighboring to the boxes and triangles; also see the gray arrows pointing from before to after the flares. The thick dashed lines show $|T_w| = 2$ and the $n = 1.3$, i.e., the empirically derived thresholds, while the thin dashed line shows $|T_w| = 1$, below which the MFR does not exist. Right panels: histogram of the twist number $|T_w|_{\max}$ and the decay index n before and after flares for the two types of flares.

flares. Here we focus on how two parameters change from before to after eruptions.

Before showing the statistical results, we first give two typical examples of the variation of MFR through two flares, as shown in Figure 1. The first one is the event 26 in Table 1, an M5.2 confined flare on 2014 February 4 in AR 11967. The MFR before the flare has a coherent structure with peak twist number of $T_w = -1.9$ (see the pre-flare MFR configurations for

all the studied events in Duan et al. 2019), and after the flare it shows no evident change with the peak twist number only slightly reduced to $T_w = -1.68$. The decay index at the apex of the MFR is $n = 1.03$ before the flare and $n = 0.96$ after. The small variation of the MFR through the flare is consistent with the confining nature of the flare. The second example is shown for event 45, an X9.3 eruptive flare on 2017 September 6 in AR 12673. As shown in Figure 1, before the flare, there is a thick,

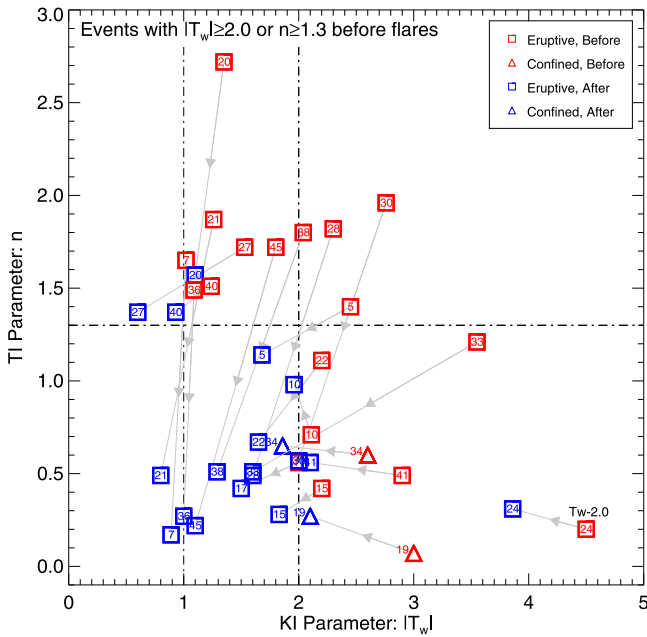


Figure 4. Same as the left panel of Figure 3, but for events with $|T_w| \geq 2.0$ or $n \geq 1.3$ before flares. Note that the pre-flare $|T_w|$ for event 24 is 6.5, and we show here $(|T_w| - 2.0)$ for a better display of the plot.

long MFR with peak twist number of $T_w = -1.8$, and it displays a good coherence and runs roughly along the main PIL of the AR. After an X9.3 flare, the MFR disintegrated, leaving a much thinner MFR with rather weak peak twist of $T_w = -1.1$, indicating that most (but not all) of the pre-flare twisted flux of the MFR erupted during the flare in this case. The remaining MFR after the flare is much lower than the pre-flare one, and thus the decay index n drops from 1.72 to 0.22. This is a clear example in which both the twist number and the decay index of the MFR decrease significantly through the eruption.

In Table 1, we list the parameters for all the events including the pre-flare peak T_w and n and their post-flare values. Figure 2 shows histograms for the distributions of the two parameters, $|T_w|_{\max}$ and n , as well as the apex height of MFR axis in all the events before and after the flares. As can be seen, on average all the parameters show a decrease through the flares; the average $|T_w|_{\max}$ decreases from 1.73 to 1.37; the average n decreases from 0.88 to 0.63, and the average apex height of MFRs is lowered from $15''$ to $7''$. We note that, as shown in the $|T_w|_{\max}$ distribution, a majority of the events (32 in 45, or 71%, which is comparable to the pre-flare percent of 87%) after the flare still have MFRs using our strict definition (i.e., magnetic flux with $|T_w| > 1$), suggesting that MFRs existing after flares is rather common.

Figures 3 (left panel) and 4 show the scatter diagrams of decay index n versus $|T_w|_{\max}$ in two regimes for a better inspection. Specifically, in Figure 3, we show all the events with $|T_w|_{\max} < 2.0$ and $n < 1.3$ before the flares, which are below the thresholds ($|T_w|_{\text{crit}}$ and n_{crit}) empirically derived in our previous survey (Duan et al. 2019) and thus are not likely triggered by the ideal instabilities. There are in total 25 events (14 confined and 11 eruptive) in this regime of parameter space. From the overall change of the pre-flare values (colored in red) to their post-flare ones (colored in blue) of the two parameters, one can see the events distribute rather randomly in the region bounded by $0 < n < 1.3$ and $0.5 < |T_w| < 2$ without a systematic decrease in either the twist number or the decay

index. There are only two confined events, i.e., event 4 and event 18, in which the post-flare decay index n increases to above the threshold slightly. In the right panels of Figure 3, we show the histograms of the two parameters before and after flares for the two types of events separately. Again, there is no systematic difference between the eruptive and confined flares, indicating that the two parameters and their changes are unable to discriminate the type of flare if both of them are lower than the thresholds. This is consistent with the conclusion in Duan et al. (2019), which showed that the triggering mechanisms of the events that fall in this domain of the parameter space are not related to the ideal instabilities.

In contrast, Figure 4 shows the events with pre-flare $|T_w|_{\max} \geq 2.0$ or $n \geq 1.3$, namely, the ones with pre-flare KI or TI parameter (in some cases like events 5, 28, 30, and 38, both KI and TI parameters) exceeding their thresholds. In this domain of parameter space, we have in total 20 events, of which 18 are eruptive. Very clear and distinct from the distributions in Figure 3 (left panel), the events that we can see show systematic decrease in either $|T_w|_{\max}$ or n from through flares. Furthermore, in most of the events (18 out of 20, or 90%), both parameters after flares decrease to close to or lower than their thresholds, i.e., most of the blue marks as seen in the figure concentrate on the lower-left quadrant with $n < 1.3$ and $T_w < 2$, except events 20 and 24. These results, again, are highly consistent with and support our previous statistics (Duan et al. 2019), i.e., the thresholds for KI and TI parameters ($|T_w|_{\max} \geq 2.0$ and $n \geq 1.3$) are reasonable, and these events are very likely triggered by the ideal instabilities. It is also worth noting that most of the eruptive events have MFR after flares by our strict definition (i.e., with $|T_w| > 1$), which indicates that the pre-flare MFR often does not expel out entirely during eruption.

4. Summary

In this Letter, we systematically studied the coronal magnetic field changes, focusing on MFRs, before and after solar flares for 45 major flare events, including 29 eruptive ones and 16 confined ones. Using the CESE-MHD-NLFFF method with SDO/HMI vector magnetograms as input, we reconstructed the coronal magnetic fields immediately prior to and after the flares for all events. Then we searched the MFR for each event using a strict definition of MFRs based on 3D distribution of magnetic twist number (i.e., the MFR must have a coherent group of magnetic flux with twist number of $|T_w| \geq 1$ of constant sign), and found that while most events possess pre-flare MFRs, the post-flare MFRs are also very common in a high percent (71%) of the events. Furthermore, we calculated the two controlling parameters of ideal MHD instabilities of MFR, i.e., the maximum twist number $|T_w|_{\max}$, which controls KI, and the decay index n of the strapping field that controls TI. For all the events, the average values for the two parameters show decrease from before to after flares, with the average $|T_w|_{\max}$ decreases from 1.73 to 1.37 and the average n decreases from 0.88 to 0.63, indicating of magnetic twist releasing and MFR height decreasing through flares.

A key difference of the variation of the two parameters from before to after flare is shown in the two different regimes defined by the KI and TI thresholds derived in our previous study (Duan et al. 2019), which are $|T_w|_{\text{crit}} = 2$ and $n_{\text{crit}} = 1.3$, respectively. For the events with both parameters before flares below their thresholds, most of them after flares are also lower

than their thresholds, without systematic change of the parameters found from before to after the flares, and the two parameters and their changes are unable to discriminate the eruptive or confined type of flares. While for the events with any of the two parameters exceeding their threshold before flare, there is systematic decrease in either $|T_w|_{\max}$ or n after flare, and in most of these events, both parameters decrease to close to or lower than their thresholds. Thus, the pre-flare to post-flare changes of the two parameters confirm our empirically derived thresholds for KI and TI (i.e., $|T_w|_{\text{crit}} = 2$ and $n_{\text{crit}} = 1.3$), above which these events are very likely triggered by the ideal instabilities and can be eruptive. While for those with the two parameters below the thresholds, other eruption mechanisms such as the reconnection-based ones should be considered in order to understand the triggering of the flares and the conditions determining the eruptive or confined types. These results give a strong constraint for the values of the instability thresholds, and also stress the necessity of exploring other eruption mechanisms in addition to the ideal MHD instabilities.

This work is jointly supported by the B-type Strategic Priority Program XDB41000000 funded by the Chinese Academy of Sciences, National Natural Science Foundation of China (U2031108) and the startup funding (74110-18841214) from Sun Yat-sen University. C.W.J. acknowledges support by National Natural Science Foundation of China (41822404, 41731067, 41574170, 41531073). Z.J.Z. is supported by NSFC grant 42004142. Data from observations are courtesy of NASA SDO/AIA and the HMI science teams. Special thanks to the anonymous referee for invaluable comments and suggestions that improved the paper.

ORCID iDs

Aiying Duan  <https://orcid.org/0000-0002-1916-1053>
 Chaowei Jiang  <https://orcid.org/0000-0002-7018-6862>
 Zhenjun Zhou  <https://orcid.org/0000-0001-7276-3208>
 Xueshang Feng  <https://orcid.org/0000-0001-8605-2159>
 Jun Cui  <https://orcid.org/0000-0002-4721-8184>

References

- Alt, A., Myers, C. E., Ji, H., et al. 2020, arXiv:2010.10607
 Antiochos, S. K., DeVore, C. R., & Klimchuk, J. A. 1999, *ApJ*, **510**, 485
 Aulanier, G. 2014, in IAU Symp. 300, Nature of Prominences and their role in Space Weather, ed. B. Schmieder, J.-M. Malherbe, & S. T. Wu (Cambridge: Cambridge Univ. Press), 184
 Aulanier, G., Török, T., Démoulin, P., & DeLuca, E. E. 2010, *ApJ*, **708**, 314
 Bateman, G. 1978, MHD Instabilities (Cambridge, MA: MIT Press)
 Baty, H. 2001, *A&A*, **367**, 321
 Berger, M. A., & Prior, C. 2006, *JPhA*, **39**, 8321
 Bobra, M. G., Sun, X., Hoeksema, J. T., et al. 2014, *SoPh*, **289**, 3549
 Chen, J. 1989, *ApJ*, **338**, 453
 Démoulin, P., & Aulanier, G. 2010, *ApJ*, **718**, 1388
 Duan, A., Jiang, C., He, W., et al. 2019, *ApJ*, **884**, 73
 Fan, Y. 2010, *ApJ*, **719**, 728
 Fan, Y., & Gibson, S. E. 2003, *ApJL*, **589**, L105
 Fan, Y., & Gibson, S. E. 2007, *ApJ*, **668**, 1232
 Forbes, T. G., Linker, J. A., Chen, J., et al. 2006, *SSRv*, **123**, 251
 Hoeksema, J. T., Liu, Y., Hayashi, K., et al. 2014, *SoPh*, **289**, 3483
 Hood, A. W., & Priest, E. R. 1981, *GApFD*, **17**, 297
 Janvier, M., Aulanier, G., & Démoulin, P. 2015, *SoPh*, **290**, 3425
 Jiang, C., & Feng, X. 2013, *ApJ*, **769**, 144
 Jing, J., Liu, C., Lee, J., et al. 2018, *ApJ*, **864**, 138
 Kliem, B., & Török, T. 2006, *PhRvL*, **96**, 255002
 Kuperus, M., & Raadu, M. A. 1974, *A&A*, **31**, 189
 Liu, R. 2020, *RAA*, **20**, 165
 Liu, R., Kliem, B., Titov, V. S., et al. 2016, *ApJ*, **818**, 148
 McCauley, P. I., Su, Y. N., Schanche, N., et al. 2015, *SoPh*, **290**, 1703
 Moore, R. L., Sterling, A. C., Hudson, H. S., & Lemen, J. R. 2001, *ApJ*, **552**, 833
 Myers, C. E., Yamada, M., Ji, H., et al. 2015, *Natur*, **528**, 526
 Pesnell, W. D., Thompson, B. J., & Chamberlin, P. C. 2012, *SoPh*, **275**, 3
 Schmieder, B., & Aulanier, G. 2012, *AdSpR*, **49**, 1598
 Schmieder, B., Démoulin, P., & Aulanier, G. 2013, *AdSpR*, **51**, 1967
 Shibata, K., & Magara, T. 2011, *LRSP*, **8**, 6
 Titov, V. S., & Démoulin, P. 1999, *A&A*, **351**, 707
 Török, T., Berger, M. A., & Kliem, B. 2010, *A&A*, **516**, A49
 Török, T., & Kliem, B. 2003, *A&A*, **406**, 1043
 Török, T., & Kliem, B. 2005, *ApJL*, **630**, L97
 Török, T., & Kliem, B. 2007, *AN*, **328**, 743
 Török, T., Kliem, B., & Titov, V. S. 2004, *A&A*, **413**, L27
 Wiegmann, T. 2004, *SoPh*, **219**, 87
 Zhou, Z., Cheng, X., Zhang, J., et al. 2019, *ApJL*, **877**, L28
 Zuccarello, F. P., Aulanier, G., & Gilchrist, S. A. 2015, *ApJ*, **814**, 126